PAPER

Regarding the optimization of O1-mode ECRH and the feasibility of EBW startup on NSTX-U

View the article online for updates and enhancements.

Regarding the optimization of O1-mode ECRH and the feasibility of EBW startup on NSTX-U

N A Lopez[1] and **F M Poli**[2]

[1] Department of Astrophysical Sciences, Princeton University, Princeton, NJ 08544, United States of America
[2] Princeton Plasma Physics Laboratory, Princeton, NJ 08543, United States of America

E-mail: nlopez@pppl.gov

Abstract

Recently published scenarios for fully non-inductive startup and operation on the National Spherical Torus eXperiment Upgrade (NSTX-U) (Menard *et al* 2012 *Nucl. Fusion* **52** 083015) show Electron Cyclotron Resonance Heating (ECRH) as an important component in preparing a target plasma for efficient High Harmonic Fast Wave and Neutral Beam heating. The modeling of the propagation and absorption of EC waves in the evolving plasma is required to define the most effective window of operation, and to optimize the launcher geometry for maximal heating and current drive during this window. Here, we extend a previous optimization of O1-mode ECRH on NSTX-U to account for the full time-dependent performance of the ECRH using simulations performed with TRANSP. We find that the evolution of the density profile has a prominent role in the optimization by defining the time window of operation, which in certain cases may be a more important metric to compare launcher performance than the average power absorption. This feature cannot be captured by analysis on static profiles, and should be accounted for when optimizing ECRH on any device that operates near the cutoff density. Additionally, the utility of the electron Bernstein wave (EBW) in driving current and generating closed flux surfaces in the early startup phase has been demonstrated on a number of devices. Using standalone GENRAY simulations, we find that efficient EBW current drive is possible on NSTX-U if the injection angle is shifted below the midplane and aimed towards the top half of the vacuum vessel. However, collisional damping of the EBW is projected to be significant, in some cases accounting for up to 97% of the absorbed EBW power.

Keywords: electron cyclotron, startup, spherical tokamak, electron Bernstein wave

(Some figures may appear in colour only in the online journal)

1. Introduction

Spherical tokamaks (STs) [1–4] are a promising fusion reactor design due to their reduced aspect ratio and increased plasma β, the ratio of plasma kinetic pressure to magnetic pressure. Compared to conventional tokamaks, STs feature improved MHD stability, and their projected higher neutron fluence makes them an attractive option for testing reactor components [5, 6] or for use in fission–fusion hybrid schemes [7, 8].

By design, STs do not have much room for a central solenoid, which limits the utility of traditional Ohmic startup. Therefore, an active area of ST research is the demonstration of fully non-solenoidal startup and operation. A promising technique for non-solenoidal startup uses the electron Bernstein wave (EBW) to drive current and generate closed flux surfaces [9]. The EBW damps strongly at harmonics of the electron cyclotron frequency, even at the low temperatures typical of startup [10]. However, being predominantly an electrostatic wave, the EBW cannot propagate in vacuum. To excite the EBW by external means, a mode-conversion from injected EC waves is required [9, 11].

Consider an EC wave with O-mode polarization injected from the magnetic low-field-side (LFS) into a low density startup plasma. This O-mode wave will propagate

towards the inner wall and reflect with a mixed O- and X-mode polarization. The reflected X-mode component will then propagate from the inner wall towards the upper hybrid resonance (UHR), where it will subsequently mode-convert to the EBW and damp at the Doppler-shifted cyclotron resonance (CR). Meanwhile, the reflected O-mode component will propagate back towards the LFS, largely unabsorbed. The conversion from O- to X-mode should be close to 100% to maximize the power converted to the EBW. This can be achieved using grooved mirrors on the centerstack, as successfully demonstrated on MAST [12, 13] where up to 73 kA of EBW driven current has been achieved with 100 kW of injected power.

In principle, the EC power absorption at the UHR may be large enough to ensure plasma breakdown, as demonstrated in basic plasma physics devices [14, 15] and in large aspect ratio tokamaks, where breakdown can be achieved with a toroidally-inclined EC injection [16]. Recent simulations for National Spherical Torus eXperiment Upgrade (NSTX-U) [4] have indicated that EC pre-heating can substantially improve the current drive efficiency of RF waves [17]. There is therefore general interest in understanding how the effectiveness of the EC can be improved for synergy applications, especially in those cases where the geometry of the mirror is fixed and the same injection angle must optimize both the breakdown current and the plasma heating during the ramp-up phase.

Since the time-evolution of a plasma discharge is a highly coupled, multi-physics problem, a proper optimization scheme should incorporate figures of merit that evaluate performance over the entire shot duration rather than at a single time. Specifically, an optimization of EC performance should consider the change in absorption properties of the target plasma as it evolves in response to the applied RF power. Similarly, during the startup phase the target plasma may move significantly as it settles to an equilibrium position within the vacuum chamber. A proper optimization of EC performance should consider the non-stationarity of the target plasma as well.

In this work, we present an optimization of fundamental harmonic O-mode (O1-mode) EC Resonance Heating (ECRH) and EC Current Drive (ECCD) on NSTX-U at full field of 1 T (machine axis). This work extends a previous study of O1-mode ECRH on NSTX-U [18] by incorporating the full time-dependent performance of the ECRH into the analysis, and including ECCD within the optimization figure of merit (FoM). Integral to this study are time-dependent simulations performed with the transport solver TRANSP [19], which self-consistently evolves the plasma equilibrium and temperature profile in the presence of the injected RF power. The ECRH and ECCD calculations are performed with the ray tracing code GENRAY [20, 21] as a coupled module within the TRANSP framework.

Using standalone GENRAY simulations, we also assess the feasibility of EBW startup on NSTX-U. Although a quantitative optimization of the launcher geometry for EBW startup is not yet possible due to the inability to simulate the

formation of closed flux surfaces within the TRANSP/ GENRAY framework, qualitative constraints can still be placed on the launcher geometry based on simple physical principles. Although this study is performed on the geometry, equilibrium, and kinetic profiles of NSTX-U, the approach and results are applicable to any ST, and can easily be extended to inform an ST-based reactor design.

This paper is organized as follows: in section 2 we briefly describe the simulation setup used for the ECRH optimization. Section 3 presents the ECRH simulation results following a broad scan over injection angle, introduces the FoM used to asses launcher performance, and discusses the results of the ECRH optimization. Section 4 introduces the EBW startup simulations and presents the results of a parameter scan over poloidal injection angle and vertical launch position, while section 5 summarizes and discusses future work.

2. Simulation details

Previous ray tracing calculations concluded that on NSTX-U, the first-pass absorption (FPA) for X2-mode ECRH at 0.5 T is optimized at a launch angle of 5° downward and 1° in the toroidal direction [22], and the FPA for O1-mode ECRH at 1 T is optimized at a launch angle of 1.5° upward and 1.5° in the toroidal direction [18] with respect to the plasma normal. As this analysis was conducted for a static set of plasma parameters, it is unclear if the proposed launch angle will remain optimal throughout the EC phase as the plasma evolves in response to the injected EC power, and as the changing density profile continuously modifies the accessibility of the ECRH. The former configuration has been used in time-dependent simulations [17] with O-mode, which demonstrated that the optimal injection angle for 0.5 T provides good heating efficiency and FPA also at 1 T. However, these simulations also indicated a need for current drive, while the launcher configuration was optimized for pure heating. Increasing the ECCD is therefore a necessary goal of the new optimization effort undertaken here. Also, since the mirror geometry will be fixed, it may be more economical at times to optimize the plasma discharge evolution as a means to improve the EC performance. Only time-dependent simulations can explore such possibilities.

The TRANSP simulations evolve the equilibrium and current profile using the fixed-boundary TEQ inverse solver [23], and evolve the electron and ion thermal transport using the MultiMode MMM7.1 [24] model, based on the assessment presented in [17]. The total plasma current is fully prescribed as a function of time by the experimental measurements. The EC contribution is calculated within GENRAY using a fully relativistic, collisionless model in a toroidal field geometry [25] with momentum conserving corrections [26]. GENRAY uses 48 concentric rays to model a beam, with a divergence adjusted to reproduce the expected waist at the resonance location. The EC launcher is assumed
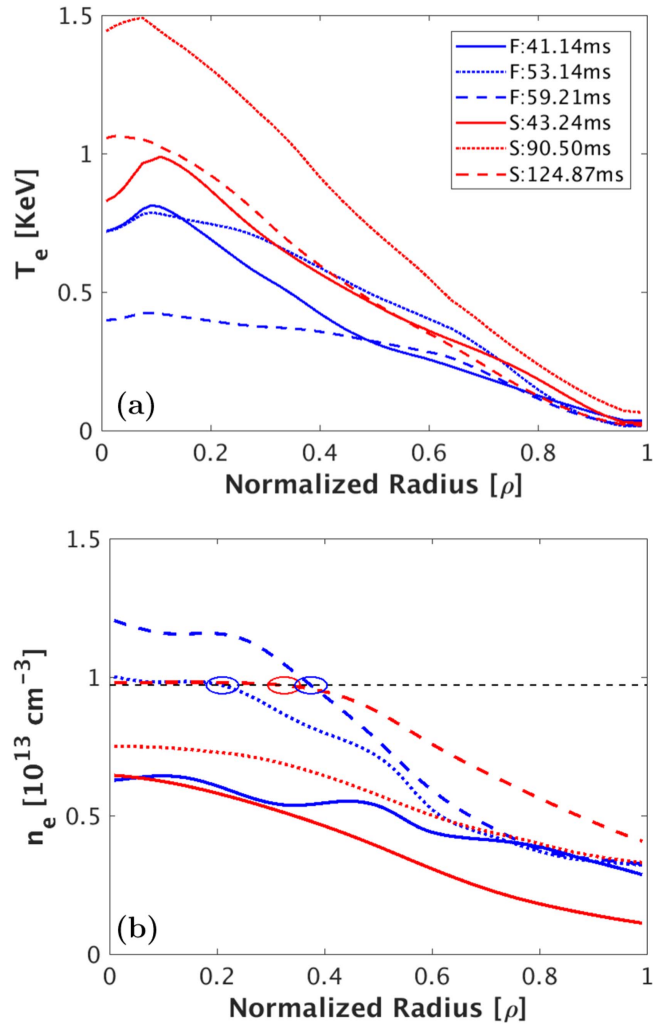
Figure 1. Temperature profiles (a) and density profiles (b) at selected times for the fast rampup scenario (blue) and the slow rampup scenario (red). Shown in dashed black is the cutoff density for 28 GHz, 9.7×10^{12} cm^{-3}. For clarity, the locations where the density profiles cross the cutoff density are circled in their respective colors. The temperature and density profiles are taken from simulations using the injection angle $(-1°, 5°)$. Being a *prescribed* quantity, the density evolution will be the same for all injection angles; conversely, being a *predicted* quantity, the temperature evolution will be different for each injection angle. The radial coordinate used is the normalized toroidal flux $\rho \doteq \sqrt{\frac{\psi(r)}{\psi(a)}}$.

to be fixed at the geometric midplane on the LFS at major radius $R = 2$ m.

For this optimization study, two different rampup scenarios are considered for the density evolution, both based on experimental observations. In the first case, henceforth referred to as the 'slow' rampup scenario, the plasma becomes overdense after approximately 125 ms. In the second case, conversely titled the 'fast' rampup scenario, the plasma becomes overdense after about 60 ms. For reference, the cutoff density at 28 GHz is 9.7×10^{12} cm^{-3}. In both cases, the entire 2-D profiles are prescribed by the experimental measurements, and are shown in figure 1.

3. O1-mode ECRH Optimization

3.1. Angular scan details and results

To characterize the effect of injection angle on the EC power absorption and CD efficiency, an angular scan $\{(\phi, \theta)|\phi \in [0, 4°], \theta \in [−7, 7°]\}$ has been conducted for each rampup scenario, where the toroidal angle ϕ is taken with respect to the plasma normal and positive in the direction of the vacuum toroidal field, and the poloidal angle θ is taken with respect to the geometric midplane and positive above the midplane. The vacuum toroidal field is oriented counter-clockwise when viewed from above, while the plasma current is oriented clockwise. Thus, the magnetic field lines are pitched towards the $(+\phi, −\theta)$ quadrant for all simulations considered in this work.

As in the previous optimization efforts [18, 22], only the first pass is considered. The working definition of 'first pass analysis' used in this paper is that each ray traverses the resonance layer a maximum of 1 time. To be consistent with this definition, the maximum toroidal injection angle is limited to 4°. This ensures the injected power does not pass tangential to the center stack and re-enter the plasma, contaminating the 'first pass' results output by GENRAY with an effective second pass.

Moreover, this constraint on the angular scan ensures that the optimal ECRH injection angle that will also be serviceable for EBW startup. To clarify, at the low densities characteristic of startup, a large fraction of the EC power will shine-through and will be reflected from the inner wall. In fact, for effective EBW startup, large power reflection will be necessary to achieve breakdown. As time progresses and the plasma density builds-up, the fraction of EC power that shines-through will decrease, while the fraction of EC power that is absorbed at the CR will increase. It is at this time when optimizing the O1-mode FPA becomes desirable. However, simulating the sequence of mode-conversions that constitutes the EBW startup is not yet possible with the GENRAY code, meaning EBW startup cannot be simulated within the TRANSP/ GENRAY time-dependent framework. To this end, only the O1-mode injection phase will be analyzed in time-dependent simulations with the aim to optimize the O1-mode FPA, while the EBW startup phase will be analyzed separately (see section 4).

The results of the angular scans are shown in figure 2. In the figure, the time-averaged ECCD and the FPA percentage for both rampup scenarios are shown as functions of the injection angle. The time-interval over which the time-averaging is performed is [27, 60] ms and [27, 125] ms for the fast and slow rampups respectively. Also shown as black contours in figure 2 are the results of fitting a Gaussian function to the EC power deposition profiles: the time-averaged flux coordinate for the peak deposition location is shown as the black contour lines in the ECCD plots, while the time-averaged Full Width at Half Maximum (FWHM) is shown as the black contour lines in the FPA plots. For convenience, both are re-scaled by a factor of 100.
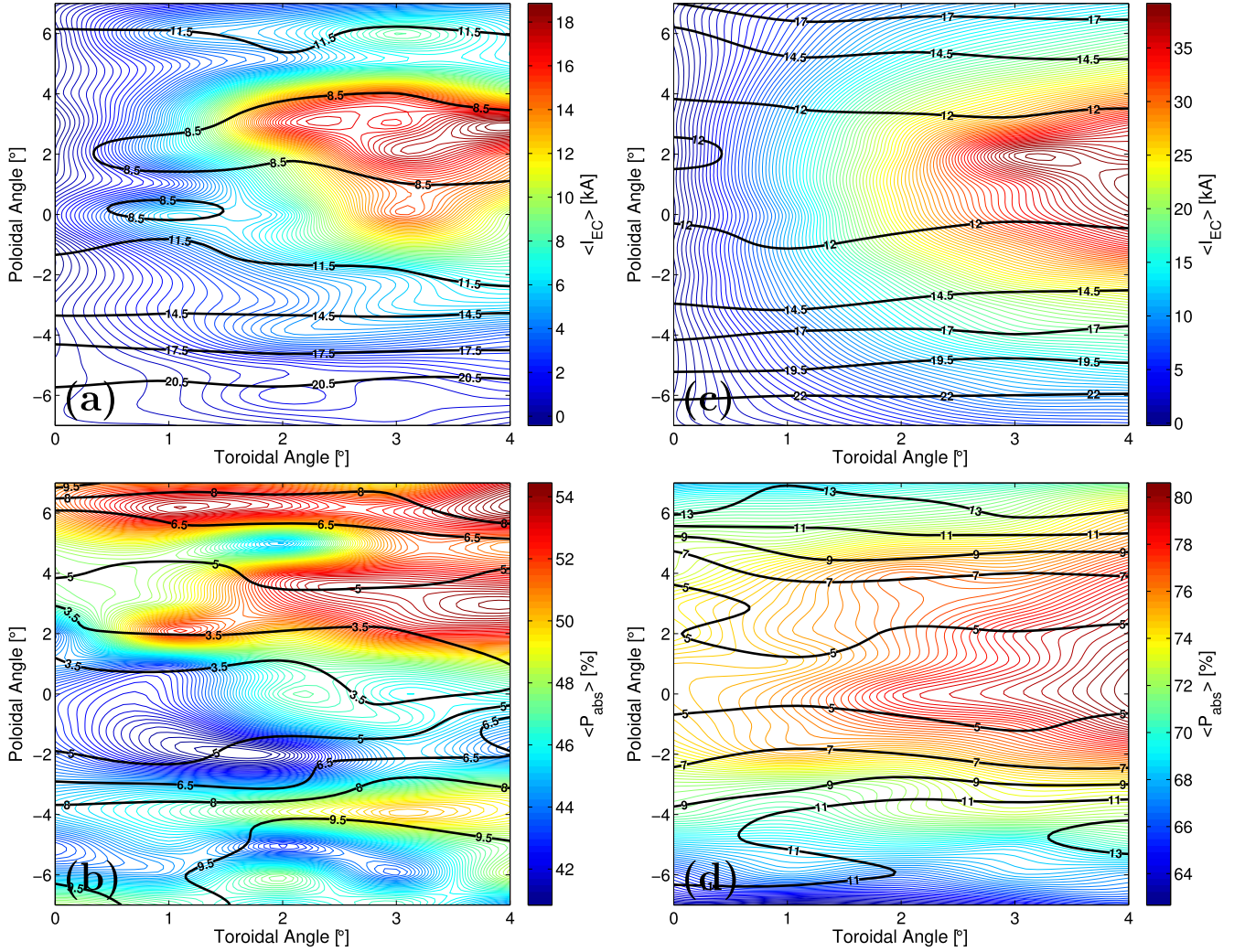
Figure 2. (a) and (b) Contour plots obtained for the fast density rampup scenario. (c) and (d) Contour plots obtained for the slow density rampup scenario. For both rampup scenarios, shown from top to bottom are the driven current and the first-pass absorption percentage as functions of the injection angle. The black contours in the ECCD plots depict the flux coordinate for the peak power deposition location, while the FWHM for the power deposition is shown as the black contours in the absorption plots. The black contour labels are all re-scaled by a factor of 100 for convenience. All quantities are time-averaged, with time-intervals defined as [27, 60] ms and [27, 125] ms for the fast rampup and slow rampup scenarios, respectively.

As seen in figure 2, the FPA can be optimized for both rampup scenarios with launch angles within 4° above the poloidal midplane, and shifted at least 2° in the toroidal direction. This is larger than the previously recommended angles of (1.5°, 1.5°) and (1°, −5°) that were obtained based on single time-slice analysis. Furthermore, strong, on-axis current drive can be expected within this angular region since, for EC waves with finite $n_{\parallel}$, high FPA is naturally accompanied by directed current drive [27].

The absorbed power and the driven current shown in figure 2 are asymmetric with respect to the poloidal launch angle. There are two reasons for this: the finite pitch angle of the magnetic field and consequent asymmetry in the launched $k_{\parallel}$ spectrum of the EC waves, and the upward vertical displacement of the magnetic axis from the geometric axis (about 5 cm).

Since the magnetic field lines are angled towards the $(+\phi, -\theta)$ quadrant, EC waves launched with $\theta > 0$ (θ^+ rays)

have a smaller $k_{\parallel}$ than those launched with $\theta < 0$ (θ^- rays). When $k_{\parallel}$ is identically zero, O-mode is linearly polarized along the external magnetic field; however for finite $k_{\parallel}$, O-mode develops a small, left-hand circularly polarized component. Indeed, the transverse polarization for O-mode is given as:

$$\frac{iB_x}{B_y} = -\frac{\omega_{ce}}{\omega} \frac{(\omega^2 - \omega_{pe}^2)N_{\parallel}^2}{\omega_{ce}^2 N_{\perp}^2 + (\omega^2 - \omega_{pe}^2)N_{\parallel}^2}. \tag{1}$$

For finite $N_{\parallel}$ in the regions of propagation, $\frac{iB_x}{B_y} < 0$, meaning the transverse polarization is left-handed, which reduces the electron cyclotron damping of these waves within the resonance region.

Because of the vertical shift of the magnetic axis, the angle between a launched ray bundle and $\nabla\psi$ will be larger for θ^- rays than for the θ^+ counterparts. This has consequences when considering the continuous formulation of

Snell's law, in which the curvature of ray trajectories in an inhomogeneous medium is given by [28, 29]: $\kappa = |\nabla \log N \times \hat{k}|$. This simplifies for O-mode to be:

$$\kappa = \frac{\omega_{pe}^2}{2(\omega^2 - \omega_{pe}^2)} \left| \frac{d \log n}{d \psi} \nabla \psi \times \hat{k} \right| \qquad (2)$$

meaning an asymmetry in $\nabla \psi \times \hat{k}$ will yield an asymmetry in the curvature of the resulting ray paths.

Thus, θ^- rays will: (1) be aimed towards regions of lower electron temperature and density, (2) tend to deflect more towards the plasma periphery, and (3) have a less desirable wave polarization at the resonance region compared to θ^+ rays; accordingly, θ^- rays have a lower power absorption efficiency. A smaller $k_{\parallel}$ will also reduce the Doppler effect experienced by the θ^+ rays compared to the θ^- rays. This will cause the deposition profiles for the θ^+ rays to be narrower and more localized on-axis, a trend corroborated by the black contours in figure 2. Even if these asymmetries are small, because EC power absorption is positively-correlated with the plasma temperature [30], there is a positive feedback mechanism that causes the asymmetries to amplify with time. This can cause large differences in performance to develop as time progresses between launchers with positive and launchers with negative poloidal injection angle, even if their performance is comparable at the start of the EC phase.

The conclusion regarding positive poloidal injection angle being preferable to negative poloidal injection angle is not true for a general equilibrium. Here, the vertical displacement of the magnetic axis is in the opposite direction as the outboard poloidal magnetic field, which leaves the positive poloidal injection angles unaffected by the associated detrimental effects. If, for example, the magnetic axis were displaced below the equatorial plane rather than above, the detrimental effects of a finite $k_{\parallel}$ and of an asymmetric $\nabla \psi \times \hat{k}$ would be oppositely-oriented. It would then be more difficult to determine which effect is dominant, and consequently, whether positive poloidal injection angle remains preferable. Even more complications arise if the equilibrium is vertically non-stationary, as such an assessment must then be performed dynamically.

An interesting feature of the fast rampup scenario is the appearance of a second angular region $\{(\phi, \theta)|\phi > 1°, \theta > 4°\}$ in which strong time-averaged FPA is also observed. This peak is not observed in the slow rampup. The reason for this is entirely due to the manner in which the fast and slow density rampups approach the overdense regime.

As can be seen from equation (2), different density profiles will give rise to different ray trajectories due to the explicit $\frac{d \log n}{d \psi}$ factor through what is known generally as gradient-index lensing (GRIN lensing) [28, 31]. For the fast density rampup, the EC absorption experiences 'reflection-dominated' GRIN lensing. This is to say, when the density profile grows overdense, the radial extent of the overdense region is localized to within $\rho \lesssim 0.2$. Being highly peaked, the density gradient is large near the axis and falls off with radius. Per equation (2), these features combine such that a
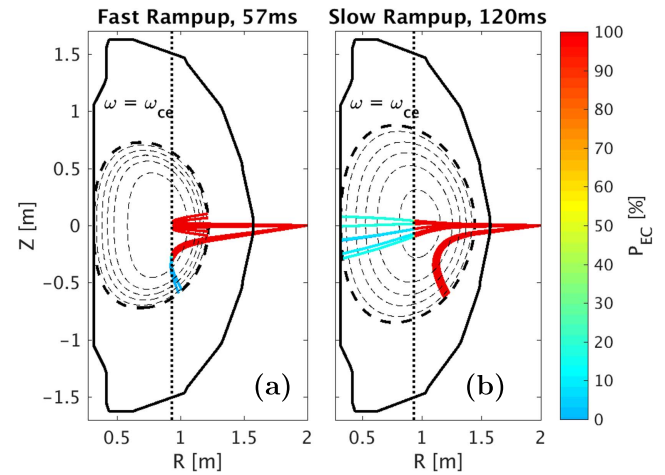

Figure 3. (a) Ray propagation in a density profile which exhibits 'reflection-dominated' gradient-index lensing. High poloidal angles can deflect under the overdense core and reach the resonance layer, while low poloidal angles are reflected. (b) Ray propagation in a density profile which exhibits 'deflection-dominated' gradient-index lensing. High poloidal angles are deflected away from the resonance layer, while low poloidal angles propagate relatively unimpeded. In both plots, all rays have non-zero power upon exiting the plasma—the reflected power is not accounted for in these simulations.

small subset of the angular region located near the poloidal midplane is severely affected by the overdense region, while injection angles with larger poloidal component are somewhat less affected and can still damp effectively at larger radius. This acts to extend the window of operation for injections at larger poloidal angle, which in turn increases the time-averaged FPA. Because the FPA for this angular region is not 'intrinsically' high, the ECCD is likewise not as high.

On the other hand, the slow density rampup experiences 'deflection-dominated' GRIN lensing. This limit is characterized by a density rampup that broadly surpasses the critical density, rather than narrowly. Therefore, all injection angles are cut off at nearly the same time. Moreover, as the density gradient is nearly constant outside $\rho \gtrsim 0.4$ and negligible within, equation (2) shows the lensing experienced by each ray results from a competition between $\nabla \psi \times \hat{k}$ and ω_{pe}^2. Within $\rho \lesssim 0.4$ the deflection is minimal; outside this central region, the deflection angle will initially increase due to the increase in $\nabla \psi \times \hat{k}$. At some point beyond $\rho = 0.4$ there will be a critical balance between the increasing $\nabla \psi \times \hat{k}$ and the decreasing ω_{pe}^2, which will result in a local maximum of the deflection angle. Beyond this point the deflection angle will decrease as the rays are launched more into the periphery of the plasma, akin to the well-known rainbow effect in particle scattering experiments [32]. Consequently as the density ramps up, larger poloidal injection angles will suffer more detrimental effects associated with beam deflection than injection angles closer to the midplane. Both of these effects, summarized in figure 3, are crucial in understanding the late-time behavior of the FPA traces shown in figure 4.
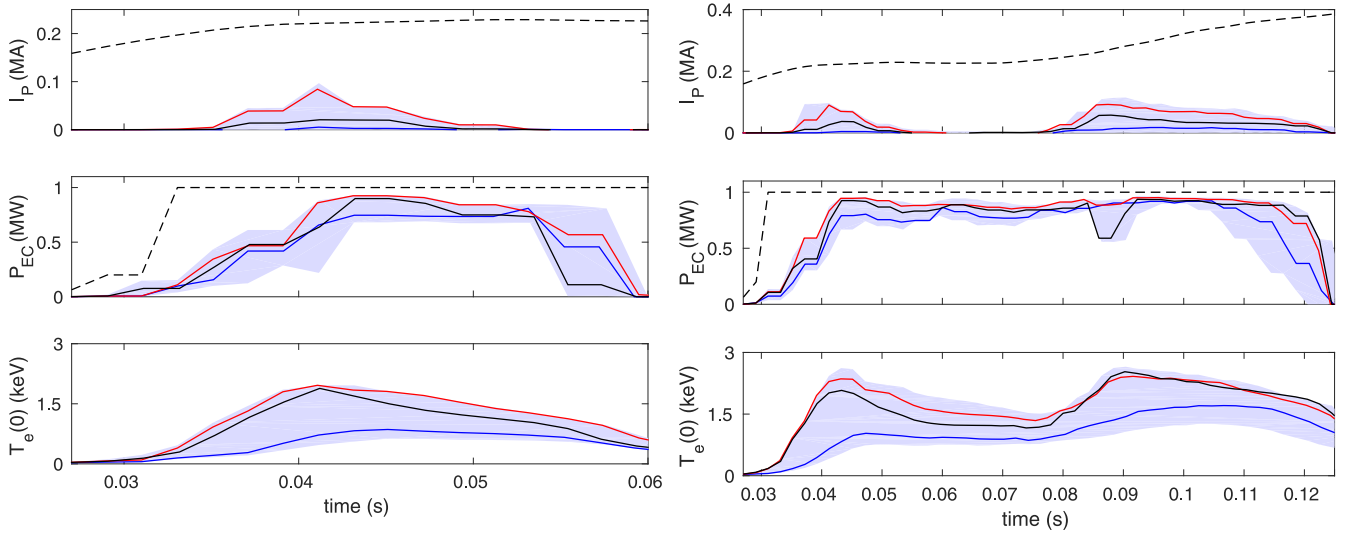
Figure 4. Comparison traces between $(1.5°, 1.5°)$ (black), $(1°, -5°)$ (blue) and $(4°, 3°)$ (red) for the fast density rampup (left) and the slow density rampup (right). From top to bottom, the ECCD, and absorbed power and the central electron temperature are shown as functions of time. The black dashed lines in the I_p and P_{EC} traces correspond to the prescribed total current, and the injected EC power, respectively. The shaded blue envelope corresponds to the total possible range of performance when considering contributions from the entire angular scan.

It is important to remark that a similar effect does not occur with respect to the toroidal injection angle. In fact, the toroidal injection angle is largely insensitive to the differences in the density rampup. This is because of the small range of the toroidal angular scan, which is set by the beam divergence and the angular width of the center stack. Presumably, this effect would be present in the toroidal injection angle as well if larger injection angles were considered.

As a second remark, since the density evolution defines the window of operation for each injection angle separately, a proper ECRH optimization should compare angles with high intrinsic FPA against those with an extended window of operation. In other words, when considering the total energy imparted to the plasma from ECRH, which can be expressed as

$$W_{EC} = \bar{P}_{EC} \Delta t \quad (3)$$

with $\bar{P}_{EC}$ the average heating rate and Δt the window of operation for a specific injection angle, then the total heating energy is maximized by maximizing $\bar{P}_{EC} \Delta t$. When the windows of operation are all equal, such as in a traditional tokamak, then the maximization of W is directly related to the maximization of $\bar{P}_{EC}$. However, if the density profile can exceed the cutoff density, such as in an ST, then Δt will not be the same for each injection angle; consequently, the maximization of W is increasingly dependent on the density profile. It is then possible that the optimal injection angle does not optimize the FPA while the plasma is underdense, but rather optimizes the window of operation. This result cannot be obtained through analysis on a single time-slice.

3.2. FoM for the optimization of the EC launch angle

An injection angle robust to modifications in the density evolution is preferable when the density evolution is an unknown quantity. For this purpose, the following FoM is used to asses launcher performance:

$$\text{FoM} = \frac{1}{6} \sum_{d=F,S} \left(\langle \tilde{I}_{EC}^d \rangle + \langle \tilde{P}_{Abs}^d \rangle + \sqrt{\frac{\langle \tilde{\Delta}^d \rangle}{2}} - 6\delta^d \right), \quad (4)$$

where the summation is over the fast and slow density rampups, the angle brackets denote time-averaging, and for a given set of values $\mathbf{O} \doteq \{O_i\}$, we have defined the normalization $\tilde{O}_i \doteq O_i / \max(\mathbf{O})$. We also define $\langle \tilde{\Delta}^d \rangle \doteq \langle \tilde{\sigma}^d \rangle + 1$, where $\langle \tilde{\sigma}^d \rangle$ is the time-averaged FWHM of the power deposition profile as obtained with a Gaussian fit. Lastly, we define $\delta^d \doteq \frac{1}{2}(N_{zone} - 1)$, where N_{zone} is the number of radial zones used in the ECCD smoothing algorithm. N_{zone} is restricted to the positive odd integers since the smoothing is symmetric about the central zone. Note also that $N_{zone} = 1$ means no additional smoothing is added to the current profiles, so there is no penalty applied to the respective launch angle.

For stability considerations, the third term in the FOM acts as a weak penalty against narrow deposition profiles. The functional form of the third term is chosen such that there is sub-linear variation in the output over the entire range of $\langle \tilde{\Delta}^d \rangle$, hence acting 'weakly' on the angular scan.

In contrast, the final term is a harsh penalty against injection angles that require additional smoothing to reach convergence in the equilibrium calculations. The justification is that the non-convergent equilibrium is interpreted conservatively as an indicator that the plasma is at risk of being driven unstable by the injected EC power. Such injection angles should therefore not be recommended. As the maximum value of the FoM is 1, any injection angle with a non-zero δ^d will be removed from consideration by this final term.

Applying equation (4) to the angular scan, the recommended ECRH injection angle that maximizes the FoM is $(4°, 3°)$. This optimal injection angle agrees with the previously established

6

Table 1. Comparison between the originally proposed injection angles of $(1.5°, 1.5°)$ and $(1°, -5°)$, and the injection angle $(4°, 3°)$. Notationally, we have introduced ρ_0 as the radial location of the maximum power deposition. Note that for $(1.5°, 1.5°)$, the quantities shown in the table are obtained after additional smoothing has been applied to the deposition profiles to ensure a convergent equilibrium.

	$(1.5°, 1.5°)$		$(1°, -5°)$		$(4°, 3°)$	
	Fast	Slow	Fast	Slow	Fast	Slow
max (FPA) (%)	89.89	93.67	80.99	92.31	92.47	95.20
$\langle$FPA$\rangle$ (%)	45.03	75.45	45.24	68.66	54.37	79.37
max(I_{EC}) (kA)	20.66	57.49	5.30	17.35	84.21	92.27
$\langle I_{EC}\rangle$ (kA)	6.22	18.86	0.78	5.36	18.99	35.03
max$(T_e(0))$ (keV)	1.88	2.53	0.86	1.71	1.96	2.42
$\langle T_e(0)\rangle$ (keV)	0.96	1.65	0.51	1.08	1.16	1.75
max(ρ_0) $[10^{-2}]$	32.86	28.47	36.45	34.03	26.18	26.07
min(ρ_0) $[10^{-2}]$	0.00	0.00	10.17	1.47	0.00	0.00
$\langle\rho_0\rangle$ $[10^{-2}]$	9.22	11.70	19.40	19.10	7.60	11.42
max(σ) $[10^{-2}]$	13.54	10.44	13.60	24.72	10.50	12.36
min(σ) $[10^{-2}]$	2.23	1.91	2.55	1.98	0.19	2.22
$\langle\sigma\rangle$ $[10^{-2}]$	4.62	4.57	8.69	11.13	4.49	5.73
δ	0	1	0	0	0	0
FoM	-0.296		0.626		0.925	

intuition that the ECRH should be launched with positive poloidal injection angle for the equilibrium under consideration.

Figure 4 compares the full time-dependent performance of the angle $(4°, 3°)$ with the previously recommended angles of $(1.5°, 1.5°)$ and $(1°, -5°)$ for both rampup scenarios. The quantities shown in the figure are the ECCD, the FPA, and the central electron temperature as functions of time. The light blue region enveloping the traces depicts the total possible range of performance resulting from the angular scan. To prevent misinterpretations of this envelope, we emphasize that the physical trajectories through this 'performance' space are non-trivial and non-monotonic. To follow a constant trajectory, such as attaining the maximum possible performance over the entire EC phase, one would need to dynamically change the EC injection angle in response to the plasma evolution.

For the fast density rampup, the windows of operation for $(4°, 3°)$ and $(1°, -5°)$ are longer than that for $(1.5°, 1.5°)$ due to reflection-dominated GRIN lensing. On the slow rampup the converse is true: $(4°, 3°)$ and $(1.5°, 1.5°)$ have longer windows of operation than $(1°, -5°)$ due to deflection-dominated GRIN lensing. Therefore, due to its intermediate poloidal injection angle, $(4°, 3°)$ optimally balances reflection- and deflection-dominated GRIN lensing. The angle $(4°, 3°)$ also provides highly localized on-axis heating, allowing central electron temperatures up to 1.96 and 2.42 keV for the respective fast and slow rampup scenarios. The large toroidal injection angle combined with high FPA allows for non-inductive current exceeding 84 and 92 kA to be obtained on the fast and slow rampups. A more detailed comparison of the three injection angles is shown in table 1. Note that $\delta = 1$ for $(1.5°, 1.5°)$ on the slow density rampup, which means that additional smoothing was needed in the equilibrium calculations. For this reason, $(1.5°, 1.5°)$ is not recommended and will not be further discussed in this paper.

Deposition profiles at selected times for $(4°, 3°)$ and $(1°, -5°)$ can be viewed in figure 5. In producing figure 5, an averaging is performed over a small range of selected time-slices. For the slow rampup, the averaging is performed over the time windows $[56, 68]$ ms and $[88, 100]$ ms, while for the fast rampup, the time windows are $[35, 39]$ ms and $[49, 53]$ ms. In both cases, the width of the averaging interval constitutes 12% of the ECRH duration. The central times for the slow rampup were selected to sample the peak and valley regions of the EC current profile, whereas the central times for the fast rampup were chosen to show the early- and late-time behavior of the ECRH, when the reflection-dominated lensing is not and is present.

The deposition of $(1°, -5°)$ tends to be spread out over a large radial region, with the current profile rapidly oscillating about zero such as to yield negligible net current. On the contrary, the deposition of $(4°, 3°)$ is well-localized within $\rho = 0.25$. A notable exception occurs in the vicinity of 60 ms on the slow rampup, in which the deposition location for all injection angles shifts outward.

Interestingly, the outward shift of the deposition location coincides with the observed dip in the I_p and T_e traces for the slow density rampup. Both the ECCD and the central electron temperature rise initially; however, beginning around 50 ms until approximately 80 ms, both suffer significant reductions in magnitude before recovering. As seen in figure 6, this time period coincides with an inward transit of the plasma flux surfaces. The magnetic axis, initially located at $R = 0.92$ m, shifts to a minimum distance of $R = 0.82$ m before moving outwards and approaching $R = 1.02$ m.

A possible mechanism to link the two-peaked I_p and $T_e(0)$ traces to the shifting plasma is given by the following argument: consider the single particle non-relativistic EC resonance condition, which can be written as:

$$v_\parallel = \frac{\omega - \omega_{ce}}{k_\parallel} \tag{5}$$

As such, resonant particles are required to have larger values of $v_\parallel$ the farther they are from the resonance layer $\omega = \omega_{ce}$. Since effective ECCD relies on the EC waves damping on particles with finite $v_\parallel$, it likewise relies upon a strong Doppler shift present in the deposition profile.

In figure 6, the magnetic axis begins at the CR and shifts to the High-Field Side (HFS). At this time, the electron temperature is a centrally-peaked function of ρ, so the CR shifts into a colder region of the plasma with a larger spatial temperature gradient. This in turn acts to reduce the Doppler effect on the incoming side of the resonance and to increase the Doppler effect on the outgoing side, resulting in partial cancellation of the driven current. This partial cancellation is further augmented by the continued inward transit of the plasma until negligible net current results. The decrease of the central electron temperature simply reflects the change in
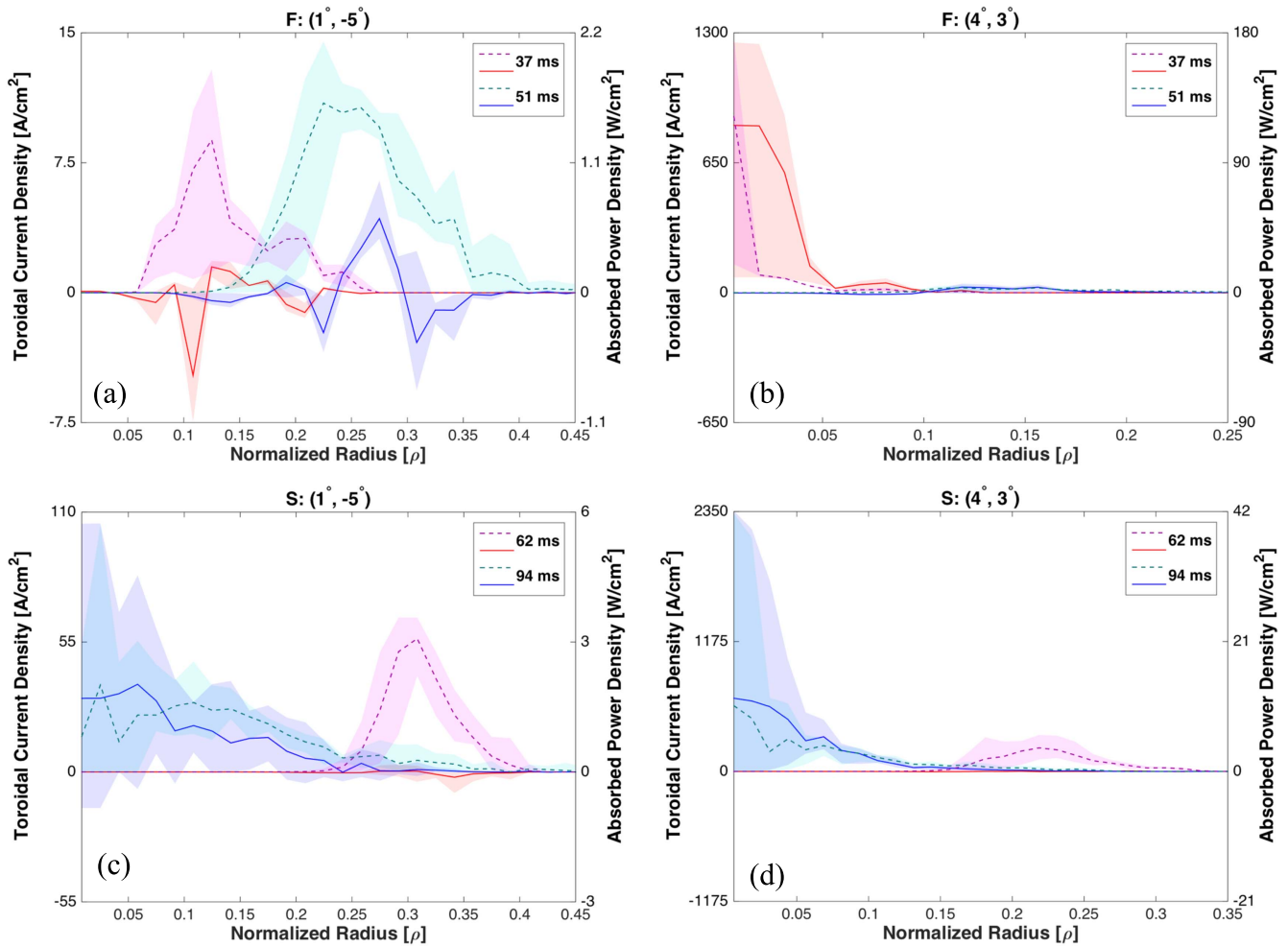
Figure 5. Radial profiles for the mean EC current density (red/blue solid lines) and the mean EC absorbed power density (pink/cyan dashed lines) at selected times. For the slow density case, the averaging is performed over the time periods [56, 68] ms and [88, 100] ms, while for the fast density case, the time periods are [35, 39] ms and [49, 53] ms. Shown in the figure legend are the central times for these intervals. The shaded envelope depicts the total variation in the respective profile over the time periods. Subplots (a), (b) correspond to the previously recommended angle $(1°, -5°)$, while subplots (c), (d) correspond to the angle $(4°, 3°)$, both for the fast and slow density rampups respectively.

deposition location as the plasma shifts laterally, as seen in figure 5.

4. EBW startup on NSTX-U

The EBW startup technique as developed on MAST [12, 13] involves a mode-conversion between the plasma O-mode and the slow X-mode facilitated by grooved polarizers installed on the walls of the centerstack; the slow X-mode then linearly converts to the EBW at the UHR. The accurate modeling of EBW startup is an area of active research, in particular the development of closed flux surfaces is not yet fully understood [33–36]. To avoid the introduction of additional assumptions, we restrict our analysis to equilibria with closed flux surfaces.

A key component to the EBW startup technique is the O–X mode conversion off the centerstack. Within GENRAY, reflections occur at the LCFS and preserve the mode character of the wave. To accurately model the O–X conversion, two

GENRAY simulations must be coupled together with the final state of the O-mode simulation determining the initial state of the X-mode simulation. There are no reflections allowed within these individual GENRAY simulations. Such a coupling is not yet available within the TRANSP framework; as such, for this section our assessment is confined to a single time-slice. The time-slice is chosen to be 27 ms for both the fast and the slow rampup scenarios since this is the earliest equilibrium available with closed magnetic surfaces.

Figure 7 shows the electron density and electron temperature profiles at 27 ms for both rampup scenarios. Notably, the electron temperature profile is hollow for both rampup scenarios at this time. Counter to the nomenclature, the slow rampup density peak is about 67% larger than the fast rampup density peak during this early startup phase, which will result in enhanced collisional and refractive effects on the wave propagation and absorption.

The following algorithm is used to couple the O-mode and X-mode GENRAY simulations: let (x_O, y_O, z_O) define the final location of the O-mode ray on the LCFS in cartesian
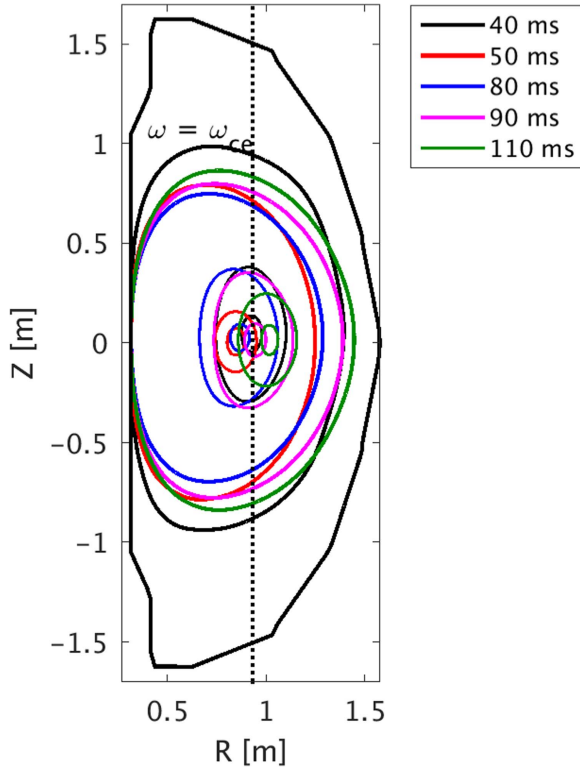
Figure 6. Snapshots of the inner plasma flux surfaces at selected times. The flux surfaces shown are $\rho = 1.0$, $\rho = 0.1$, and $\rho = 0.01$. An inward shift of the inner flux surfaces appears during a time period contemporaneous with the observed deterioration of the ECCD in the slow density rampup scenario; the resurgence of the ECCD coincides with the flux surfaces returning to their original location.
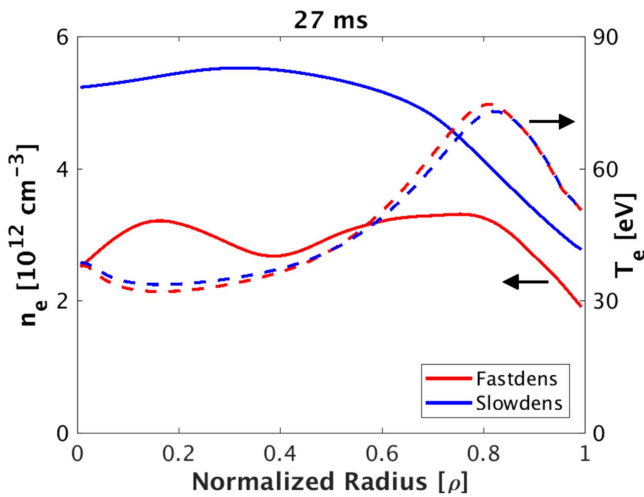

Figure 7. Electron density (solid lines) and electron temperature (dashed lines) profiles for the fast (red) and slow (blue) rampup scenarios at 27 ms.

coordinates. Let us further define $r_O \doteq \sqrt{x_O^2 + y_O^2}$ as the cylindrical radial coordinate of the final O-mode ray location, and define $\varphi \doteq \tan^{-1}\left(\frac{\Delta y}{\Delta x}\right)_O$ and $\vartheta \doteq -\tan^{-1}\left(\frac{\Delta z}{\Delta r}\right)_O$ respectively as the angles the tangent to the ray trajectory makes with the $y = 0$ and $z = 0$ planes at the LCFS. Finally, let (r_X, Φ_X, z_X) be the launch location of the converted X-mode on

the centerstack in cylindrical coordinates, and θ_X and ϕ_X be respectively the poloidal and toroidal launch angles of the converted X-mode.

Treating the Scrape-Off Layer (SOL) as vacuum to allow the use of straight-line ray trajectories, modeling the centerstack as a uniform cylinder, and assuming specular reflection holds, the following relations are derived:

$$r_X = 0.31 \text{ m} \tag{6a}$$

$$z_X = -\tan\vartheta(r_X - r_O) + z_O \tag{6b}$$

$$\theta_X = 90° - \vartheta \tag{6c}$$

$$\Phi_X = \cot^{-1}\left(\frac{A}{B - \sqrt{C \cdot D}}\right) \tag{6d}$$

$$\phi_X = \Phi_X - \varphi, \tag{6e}$$

where:

$$A = r_X^2 - D \tag{7a}$$

$$B = r_X^2 \tan\varphi \tag{7b}$$

$$C = r_X^2 \sec^2\varphi - D \tag{7c}$$

$$D = (y_O - x_O \tan\varphi)^2. \tag{7d}$$

To allow for imperfect O–X mode-conversion at the centerstack, we set:

$$P_X = C_{OX} P_O, \tag{8}$$

where P_X is the launched X-mode power, P_O is the remaining O-mode power at the LCFS, and C_{OX} is the O–X conversion efficiency of the grooved polarizers. Note that in all these expressions, spatial units are meters and angular units are degrees.

We perform an angular scan over the O-mode injection angle. Holding the toroidal angle fixed at $4°$, the poloidal angle is scanned from $-12°$ to $+12°$. As before, the launcher is located at a radial distance of 2 m on the geometric midplane ($z = 0$ m). However, a constraint within GENRAY regarding the direct launch of EBW rays limits the number of rays for each iteration of the scan to 6, rather than the full 48 used in the previous sections. This constraint arises because each EBW ray must be launched individually to account for the wide variation in initial positions resulting from finite beam divergence. Figures 8 and 9 show the ray trajectories on the fast and slow rampup scenarios for the specific injection angle ($4°$, $3°$).

Figure 10 decomposes the total injected EC power into the fraction absorbed as O-mode (red shaded region), X-mode (green shaded region), and EBW (blue shaded region). The EBW absorbed power fraction is further split into two subregions: the non-hatched blue region is the fraction of EBW power absorbed via collisionless cyclotron damping (CCD), and the hatched blue region is the fraction of EBW power absorbed via non-resonant collisional damping (NRCD), which does not drive current. The white regions denote lost power: the white region filled with horizontal bars that separates the O- and X-mode regions represents the power lost to the SOL because the reflected X-mode never re-enters the LCFS; the white region filled with diagonal bars that separates the X-mode and EBW regions represents the power
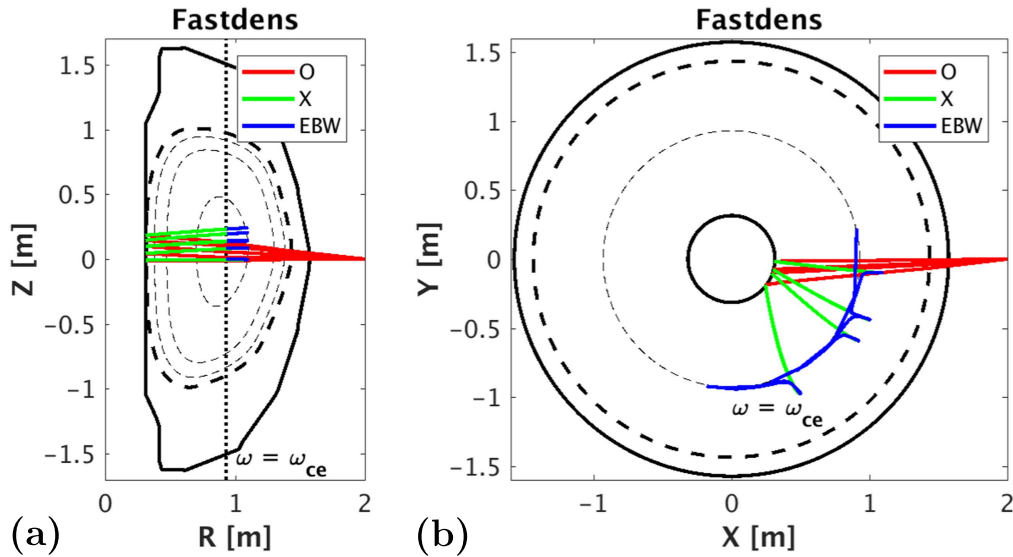
Figure 8. Poloidal (a) and toroidal (b) projections of the ray trajectories for the O–X-EBW startup scheme on the fast rampup equilibrium for the specific case of $\theta = 3°$. 6 rays are used to model the beam, and reflections off the centerstack are calculated using equations (6a)–(6e).

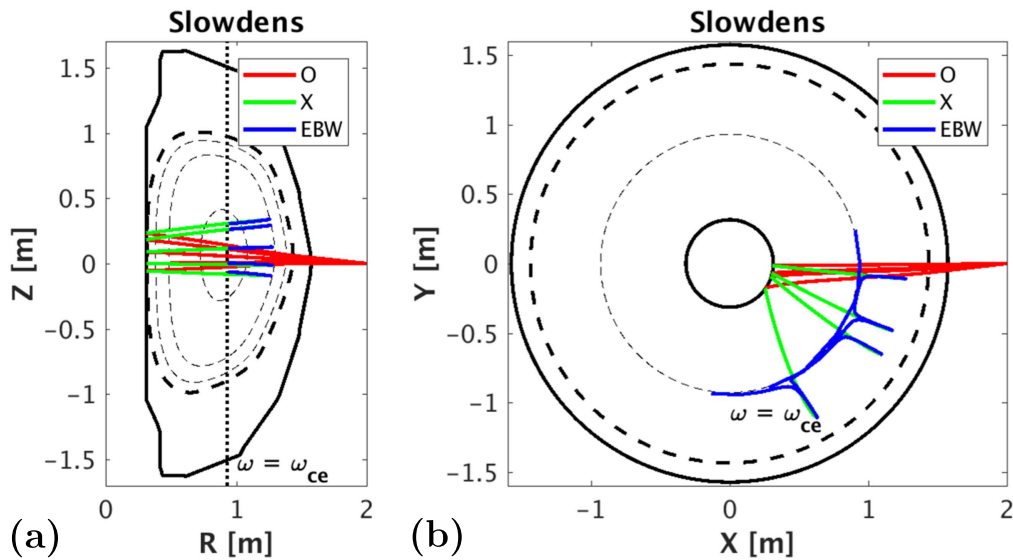**Figure 9.** Poloidal (a) and toroidal (b) projections of the ray trajectories for the O–X-EBW startup scheme on the slow rampup equilibrium for the specific case of $\theta = 3°$. 6 rays are used to model the beam, and reflections off the centerstack are calculated using equations (6a)–(6e).

lost to the SOL because the reflected X-mode successfully re-enters the LCFS, but does not subsequently encounter the UHR before exiting the plasma; finally, the white region filled with vertical lines that lies below the EBW region represents the power that remains unabsorbed after the simulation concludes by reaching the maximum number of iterations. This typically occurs for launches near the midplane where there is not a well-defined directionality to the $N_\parallel$ evolution of the EBW rays [37], and is interpreted to signify very weak damping. In generating figure 10 we assume complete O–X conversion at the centerstack ($C_{OX} = 1$), therefore all the losses to the SOL are due to geometrical considerations and not to inefficiencies of the polarizers.

From the equilibria, the electron-ion collision frequency normalized to the wave frequency is estimated to be $\frac{\nu_{ei}}{\omega} = 15.7$ for the fast rampup and $\frac{\nu_{ei}}{\omega} = 19.9$ for the slow

rampup. Both of these values are well beyond the 10^{-4} threshold established in previous works [38–41], above which collisional damping of the EBW becomes significant. Indeed, from figure 10 one sees that for injection angles near the midplane, up to 97% of the absorbed EBW power can be from NRCD.

The ECCD modules available within GENRAY are derived under the assumption that the normalized collision-ality is small, i.e. $\nu_e^* \ll 1$, where ν_e^* is the ratio between the electron detrapping frequency and the electron bounce frequency. However, following [42] we estimate $\nu_e^* = 76.5$ for the fast rampup scenario and $\nu_e^* = 87.8$ for the slow rampup scenario at 27 ms, meaning the collisionless ECCD modules are insufficient for the equilibria under consideration. One should therefore employ a Fokker-Planck solver to properly calculate the plasma current in this collisionality regime. With
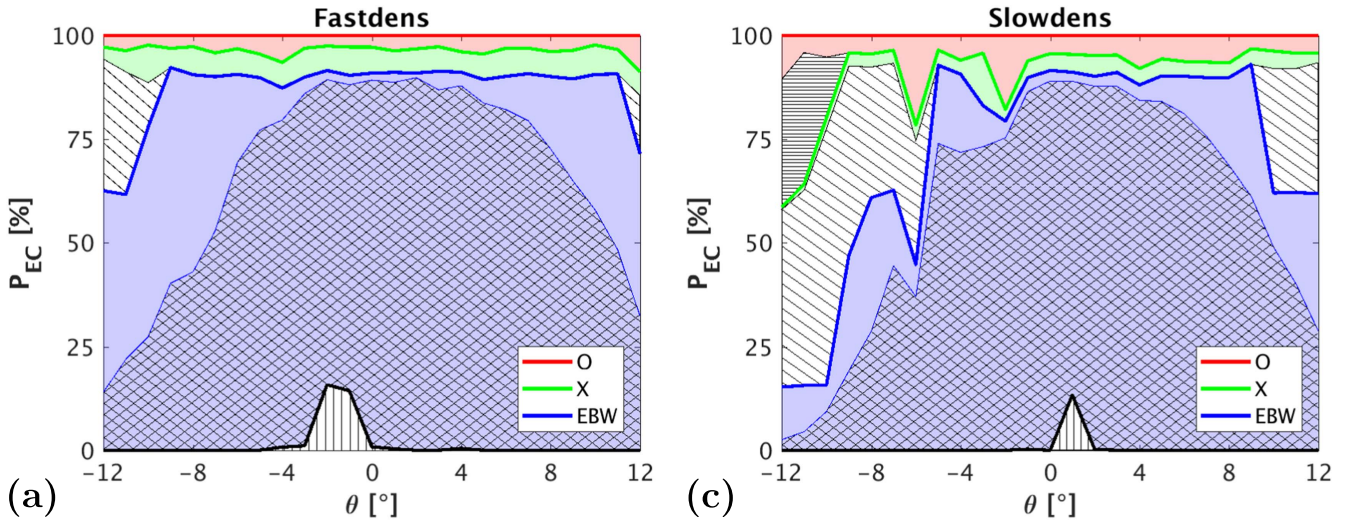
Figure 10. Fraction of initial EC power absorbed as O-mode (red), X-mode (green), and EBW (blue) with respect to poloidal injection angle for the fast (a) and slow (b) rampup scenarios assuming complete O–X conversion off the centerstack. The solid colored lines and the shaded colored regions denote respectively the initial power fraction and the absorbed power fraction of the appropriate wave mode. The cross-hatched blue shaded region shows the fraction of EBW power absorbed via non-resonant collisional damping. The white region filled with horizontal bars represents the fraction of power lost to the SOL during the O–X conversion, while the white region filled with diagonal bars represents the fraction of power lost to the SOL during the X-EBW converion. Finally, the white region filled with vertical bars represents the fraction of unabsorbed power due the the simulations reaching an arbitrary maximum number of iterations.

this said, when considering the effects of finite collisionality, previous works show that the collisionless ECCD models yield a systematic underestimation of the driven current [26, 43–45]. To minimize computational cost, we therefore continue to use the collisionless ECCD calculations within GENRAY to provide a conservative estimation of the EBWCD. Assessing the effects of finite collisionality on the current drive efficiency in startup environments will be the subject of future work.

Figure 11 shows the EBWCD for both rampup scenarios as a function of the poloidal injection angle. The solid lines show the EBWCD assuming complete O–X conversion off the centerstack, the dashed lines show the EBWCD assuming 75% O–X conversion efficiency, and the dotted lines show the EBWCD assuming 50% conversion efficiency. The impact of incomplete O–X conversion off the centerstack is an overall multiplicative reduction in the EBWCD. There are three features of interest in figure 11: (1) the performance of large poloidal angles compared to small poloidal angles, (2) the rapid changes in the direction of the driven current for large negative poloidal angles, and (3) the relative performance between the fast and slow rampup scenarios.

Regarding (1), higher poloidal injection angles are more effective than lower poloidal injection angles because of the increased $N_{\parallel}$ upshift and the decreased distance between the UHR and the CR. Both of these features can be seen more easily in figures 12 and 13, which show the evolution of $N_{\parallel}$ and the flux coordinate ρ of the EBW rays along the ray trajectories. Only the central ray of each distinct poloidal injection angle is shown. Along the colored lines, the white diamond indicates the onset of NRCD, and the transition from colored line to black dotted line denotes the onset of CCD. One can see that the higher poloidal angles (red/blue lines) experience a larger $N_{\parallel}$ upshift compared to the lower poloidal angles (yellow/green/
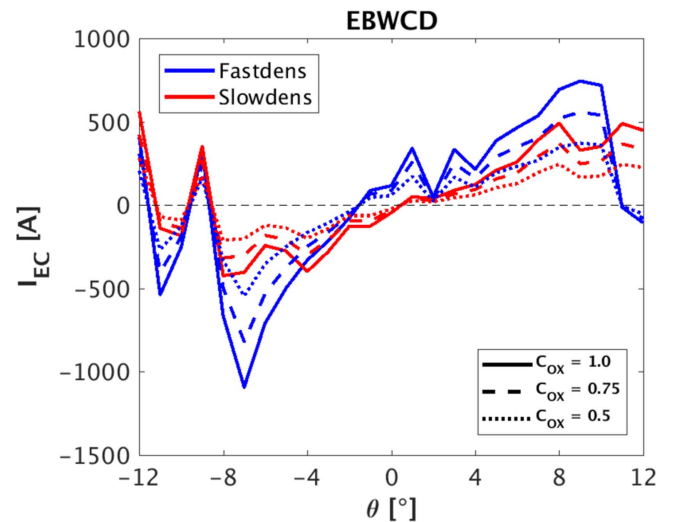

Figure 11. Non-inductive current driven by the EBW for the fast (red) and slow (blue) rampup scenarios assuming 100% (solid lines), 75% (dashed lines), and 50% (dotted lines) conversion efficiency between the O and X modes. The O–X mode conversion is facilitated by reflection off the centerstack. The dashed black horizontal line marks $I_{\text{EC}} = 0$.

light blue lines), meaning these rays will drive current with a well-defined directionality. Finite beam divergence also reduces the EBWCD for low poloidal injection angles due to the partial cancellation of the current driven by EBW rays that end above and below the geometric midplane, as seen in the ray trajectories of figures 8 and 9. The higher poloidal injection angles also have a shorter distance between the onset of NRCD and the onset of CCD, which is corroborated in figure 10 by the larger fraction of EBW power absorbed via CCD for higher poloidal injection angles.
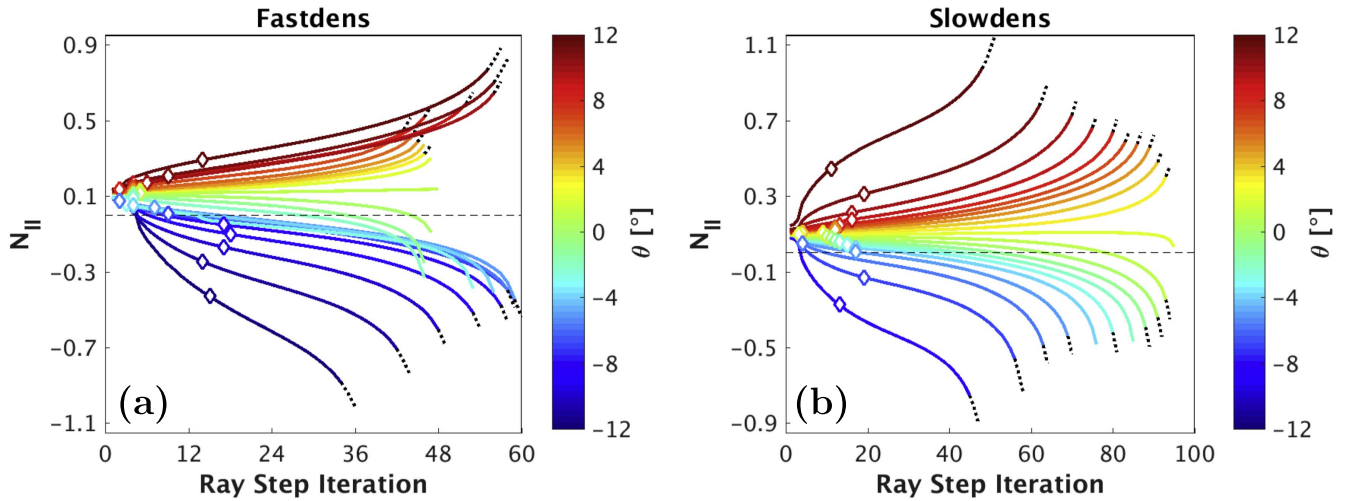
11

Figure 12. The evolution of $N_\parallel$ along the EBW rays for the fast (a) and slow (b) rampup scenario. The color of the lines corresponds to the poloidal injection angle used in the O–X-EBW mode conversion scheme. The white diamonds denote the onset of collisional damping, while the transition from a colored line style to a black dashed line style demarcates the onset of electron cyclotron damping. The dashed black horizontal line marks $N_\parallel = 0$. Only the values corresponding to the central ray are shown.
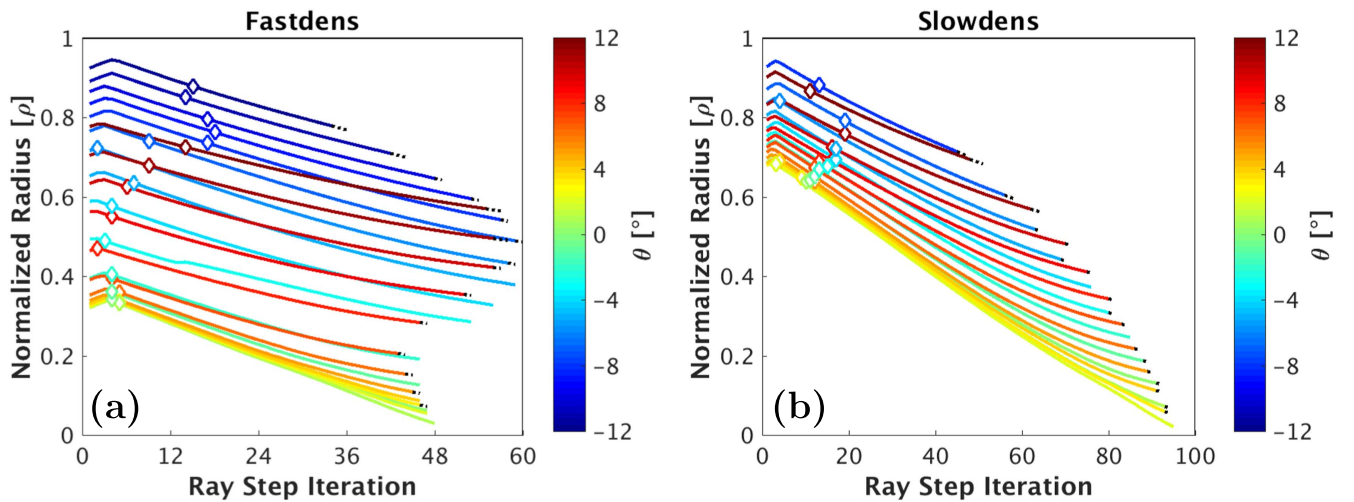

Figure 13. The evolution of ρ along the EBW rays for the fast (a) and slow (b) rampup scenario. The color of the lines corresponds to the poloidal injection angle used in the O–X-EBW mode conversion scheme. The white diamonds denote the onset of collisional damping, while the transition from a colored line style to a black dashed line style demarcates the onset of electron cyclotron damping. Only the values corresponding to the central ray are shown.

Regarding (2), the rapid variation in the directionality of the EBWCD for high negative poloidal injection angles is most likely explained by the erroneous presence of an Ohkawa effect [46]. It has been well-established in the collisionless regime that the EBW can drive significant counter-directional current via the Ohkawa mechanism because of their strong $N_\parallel$ upshift [47–49]. As mentioned previously, however, collisionless ECCD models tend to underestimate the magnitude of the driven current due to the presence of trapped particles. If present, trapped particles tend to be located predominantly on the outer flux surfaces where the mirror ratio along a field line is larger. From figure 13, the higher poloidal injection angles damp farther from the core than lower poloidal injection angles, which nominally should increase the impact of trapped particles on the

EBWCD. However, since we used a collisionless model to describe the current drive in a collisional plasma, when one corrects for the reduced population of trapped particles one expects the EBWCD to be more positive than in figure 11 for the high positive poloidal angles and more negative than in figure 11 for the high negative poloidal angles. Such a correction may be large enough to remove the rapid variation in the directionality of the EBWCD, although this remains to be investigated in future studies.

Regarding (3), the EBWCD on the slow rampup is lower than the EBWCD on the fast rampup. This is due to the previously mentioned enhanced refraction and collisionality of the slow rampup compared to the fast rampup. As seen in figure 10, the slow rampup suffers more losses to the SOL than the fast rampup. This is an effect due to
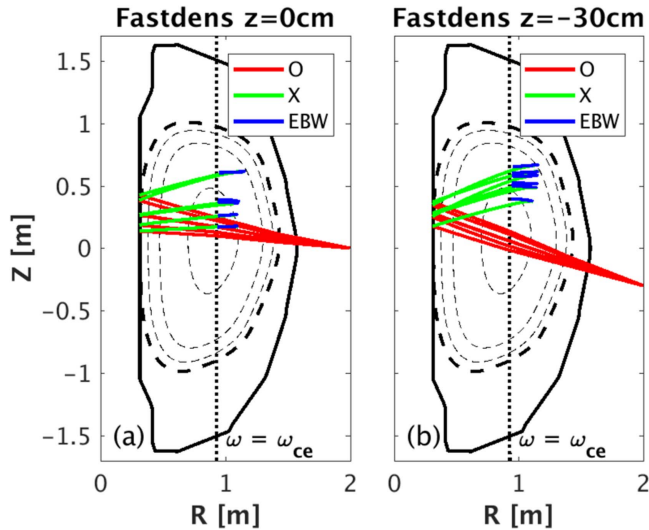
Figure 14. Comparison of ray trajectories for midplane launch (a) and for a launcher shifted below the midplane (b). The shifted launcher reduces the beam spot size at the upper hybrid layer by reducing $\nabla\psi \times \hat{k}$.

refraction—either the O-mode beam deflects too far towards the periphery of the plasma (O–X SOL loss), or the reflected X-mode deflects too far towards the periphery of the plasma (X-EBW SOL loss). As a result, there is less power in the EBW channel to drive current in the slow rampup scenario. Furthermore, as seen in figures 8 and 9, the UHR is located farther from the CR in the slow rampup than in the fast rampup because of the former's higher density. This means there is more distance over which the EBW will collisionally damp in the slow rampup, further reducing the EBWCD.

The refractive effects of the density profile can be reduced for both rampup scenarios by shifting the launcher below the midplane. As seen in figure 14, moving the launcher below the midplane reduces the EC beam spot size on the UHR. In turn, this will induce less variation in the excited EBW rays and hence, will produce a more predictable and robust EBWCD. The reduction in beam spot size is directly linked with a reduction in $\nabla\psi \times \hat{k}$ for the launched O-mode waves. Conversely, if electron current is instead desired to be driven counter-directional with respect to the toroidal field, then the EBW should be excited below the midplane. In this case, shifting the launcher above the midplane will reduce the spot size.

Optimizing the EBWCD during the startup phase is therefore best accomplished by (1) shifting the launcher below the midplane, and (2) maintaining the plasma density as low as possible for as long as possible, until the FPA of the O-mode and X-mode becomes significant. Shifting the launcher below the midplane will minimize the refractive effects of the density profile while still exciting the EBW well above the midplane, while the lower density will reduce the collisionality and shorten the distance between the UHR and the CR such that a larger fraction of the EBW power can be used to drive current. It should be noted that although NRCD does not contribute directly to driving current, it does result in

heating. For certain parameter regimes, this may result in a synergistic 'self-healing' process, as the collisional heating will reduce the collisionality and increase the efficiency of the EBWCD. The precise impact of this collisional synergy must be explored in time-dependent solutions to determine how well it might correct, say, the use of a suboptimal injection angle.

5. Conclusion

In this work, we perform an optimization of ECRH on NSTX-U using time-dependent simulations. For traditional O1-mode ECRH, two separate density rampup scenarios are considered: a fast rampup in which the plasma becomes overdense at approximately 60 ms, and a slower rampup where the plasma becomes overdense at approximately 125 ms. An angular scan is performed over the poloidal and toroidal injection angles, and it is found that there exists a broad angular region robust to modifications in the density rampup. In this region, the injection angle is shifted at least 2° in the toroidal direction and within 4° above the poloidal midplane.

For the optimization, a simple figure of merit is developed that balances the current drive and the first pass absorption achieved by each injection angle over the entire EC duration. Applying this figure of merit to the angular scan, the optimal injection angle points 3° above the poloidal midplane and 4° in the toroidal direction, which belongs to the identified class of robust injection angles.

For this optimal choice of injection angle, the deposition is peaked on-axis and as such, central electron temperatures exceeding 1.9 and 2.4 keV can be obtained for the fast and slow rampup scenarios, respectively. Additionally, this injection angle can provide up to 84 kA of ECCD on the fast rampup and 92 kA on the slow rampup cases. In light of these numbers, a slower density rampup is preferable for optimizing ECRH performance than a faster density rampup. However, deleterious effects associated with the magnetic axis shifting to the HFS of the resonance layer are observed in the slow density rampup, which result in the ECCD efficiency dropping substantially. Similarly, the time-averaged ECRH efficiency is inferred to be dependent on the vertical displacement of the magnetic axis from the equatorial plane. Such vertical and horizontal motion of the magnetic axis should thus be minimized in future experiments to maximize both the EC effectiveness and the coupling of Ion Cyclotron or High Harmonic Fast Waves to the plasma.

A notable finding in this study is the effect of the density evolution on the time-averaged EC power absorption. Because the ECRH accessibility is different for each injection angle, the duration of effective ECRH must be taken into account when optimizing ECRH with respect to the injection angle. In the fast rampup scenario, the GRIN lensing of the density evolution acts to reduce the accessibility of EC rays launched with low poloidal injection angles; conversely in the slow rampup scenario, the lensing effects limit the accessibility of EC rays launched with large poloidal injection

angles. The former we categorize as a 'reflection-dominated' density evolution, and the later as a 'deflection-dominated' density evolution. In light of this, the injection angle $(4°, 3°)$ is robust to variations in the density evolution as it belongs to a class of intermediate poloidal injection angles that provides an optimal balance between the two effects. The quantification of these late-time lensing effects should facilitate the development of a controller equation for adjusting the EC injection angle given details of the density rampup. This will be the subject of a future publication.

Additionally, a novel coupling of ray-tracing simulations is developed to assess the feasibility of EBW startup on NSTX-U. This coupling is not yet available within a time-dependent framework, which limits the analysis to a single time-slice. We find that co-directional EBWCD is best accomplished by aiming the launcher towards the top half of the vacuum vessel and shifting the launcher below the mid-plane. This setup takes advantage of the well-established $N_{\parallel}$ upshift of the EBW via the positive inclination angle, and the reduced beam spot size on the UHR via the vertical displacement of the launcher to drive well-directed, well-localized current.

Unfortunately, the relatively cold temperatures ($\sim$50 eV) and relatively high densities ($\sim 10^{12}$ cm^{-3}) typical of the startup phase mean that the plasma is moderately collisional. As such, collisional damping of the EBW appears to be a significant detriment to the feasibility of EBW startup, in some cases accounting for 97% of the absorbed EBW power. It is envisioned that certain parameter regimes will lend themselves to a synergistic collisional self-healing scheme, in which the collisional damping of the EBW heats the plasma, subsequently reducing the plasma collisionality and enhancing the EBWCD; however a quantitative assessment of this effect requires a more rigorous accounting of the impact of finite collisionality on the EBWCD efficiency in a time-dependent setting, with validation against experiments. Properly resolving the quasilinear effects of the EBW heating on the electron distribution may further improve the predicted EBWCD efficiency. These investigations will also be the subject of future work.

Acknowledgments

ORCID iDs

N A Lopez ● https://orcid.org/0000-0001-5566-3731
F M Poli ● https://orcid.org/0000-0003-3959-4371

References

[1] Peng Y K M and Strickler D J 1986 *Nucl. Fusion* **26** 769
[2] Stambaugh R D, Chan V S, Miller R L and Schaffer M J 1998 *Fusion Sci. Technol.* **33** 1
[3] Jardin S C *et al* 2003 *Fusion Eng. Des.* **65** 165
[4] Menard J E *et al* 2012 *Nucl. Fusion* **52** 083015
[5] Peng Y K M *et al* 2005 *Plasma Phys. Control. Fusion* **47** B263
[6] Peng Y K M *et al* 2009 *Fusion Sci. Technol.* **56** 957
[7] Kotschenreuther M, Valanju M P, Mahajan S M and Schneider E A 2009 *Fusion Eng. Des.* **84** 83
[8] Gryaznevich M P 2012 *AIP Conf. Proc.* **1442** 55
[9] Shevchenko V F, Baranov Y, Saveliev A, Volpe F A and Zajac J 2004 EBW current drive start-up scenario for MAST *Proc. 13th Joint Workshop on ECE and ECRH (17–20 May(Nizhny Novgorod, Russia: Institute of Applied Physics)* p 162
[10] Montes A and Ludwig G O 1986 *Plasma Phys. Control. Fusion* **28** A1765
[11] Laqua H P 2007 *Plasma Phys. Control. Fusion* **49** R1
[12] Shevchenko V F, O'Brien M R, Taylor D, Saveliev A N and MAST team 2010 *Nucl. Fusion* **50** 022004
[13] Shevchenko V F *et al* 2015 *EPJ Web Conf.* **87** 02007
[14] Podesta M, Fasoli A, Labit B, McGrath M, Muller S H and Poli F M 2005 *Plasma Phys. Control. Fusion* **47** 1989
[15] Podesta M, Fasoli A, Labit B, McGrath M, Muller S H and Poli F M 2006 *Plasma Phys. Control. Fusion* **48** 1053
[16] Stober J *et al* 2011 'Integrated operations scenarios' group members and experts *Nucl. Fusion* **51** 083031
[17] Poli F M, Andre R G, Bertelli N, Gerhardt S P, Mueller D and Taylor G 2015 *Nucl. Fusion* **55** 123011
[18] Taylor G *et al* 2015 *EPJ Web Conf.* **87** 02013
[19] Hawryluk R J 1981 An empirical approach to tokamak transport *Physics of Plasmas Close to Thermonuclear Conditions* ed B Coppi *et al* vol 1 (Brussels: Commission of the European Communities) p 19
[20] Smirnov A P and Harvey R W 1995 *Bull. Am. Phys. Soc.* **40** 1837
[21] Smirnov A P, Harvey R W and Prater R 2009 General linear RF-current drive calculation in toroidal plasma *Proc. 15th Workshop on ECE and ECRH (10–13 March (Yosemite National Park, California: World Scientific)* p 301
[22] Taylor G, Ellis R A, Harvey R W, Hosea J C and Smirnov A P 2012 *EPJ Web Conf.* **32** 02014
[23] Andre R, McCune D, Pearlstein D, LoDestro L and Meyer W H 2007 *Bull. Am. Phys. Soc.* **52** 11
[24] Rafiq T, Kritz A H, Weiland J, Pankin A Y and Luo L 2013 *Phys. Plasmas* **20** 032506
[25] Lin-Liu Y R, Chan V S and Prater R 2003 *Phys. Plasmas* **10** 4064
[26] Marushchenko N B, Beidler C D, Kasilov S V, Kernbichler W, Maassberg H, Prater R and Harvey R W 2011 *Phys. Plasmas* **18** 032501
[27] Eldridge O C 1980 On currents induced in tokamaks by Electron Cyclotron heating *Oak Ridge National Laboratory Report* ORNL/TM-7503 6821959 (https://doi.org/10.2172/6821959)
[28] Gomez-Reino C, Perez M V and Bao C 2002 *Gradient-Index Optics: Fundamentals and Applications* (Berlin: Springer)
[29] Tracy E R, Brizard A J, Richardson A S and Kaufman A N 2014 *Ray Tracing and Beyond: Phase Space Methods in Plasma Wave Theory* (New York: Cambridge University Press)
[30] Erckmann V and Gasparino U 1994 *Plasma Phys. Control. Fusion* **36** 1869

[31] Moore D T 1980 *Appl. Opt.* **19** 1035
[32] Ford K W and Wheeler J A 1959 *Ann. Phys.* **7** 259
[33] Yoshinaga T, Uchida M, Tanaka H and Maekawa T 2006 *Phys. Rev. Lett.* **96** 125005
[34] Yoshinaga T, Uchida M, Tanaka H and Maekawa T 2007 *Nucl. Fusion* **47** 210
[35] Maekawa T, Yoshinaga T, Uchida M, Watanabe F and Tanaka H 2012 *Nucl. Fusion* **52** 083008
[36] Du Toit E J, O'Brien M R and Vann R G L 2017 arXiv:1705.06701
[37] Forest C B, Chattopadhyay P K, Harvey R W and Smirnov A P 2000 *Phys. Plasmas* **7** 1352
[38] Preinhaelter J, Urban J, Pavlo P, Taylor G, Diem S, Vahala L and Vahala G 2006 *Rev. Sci. Instr.* **77** 10F524
[39] Diem S J *et al* 2009 *Nucl. Fusion* **49** 095027
[40] Diem S J, Taylor G, Caughman J B, Efthimion P C, Kugel H, LeBlanc B P, Phillips C K, Preinhaelter J, Sabbagh S A and Urban J 2009 *Phys. Rev. Lett.* **103** 015002
[41] Urban J, Preinhaelter J, Diem S J, Laqua H P, Pavlo P, Shevchenko V, Taylor G, Vahala G, Vahala L and Valovic M 2009 *J. Plasma Fusion Res. Ser.* **8** 1153
[42] Sauter O, Angioni C and Lin-Liu Y R 1999 *Phys. Plasmas* **6** 2834
[43] Luce T C, Lin-Liu Y R, Harvey R W, Giruzzi G, Lohr J M, Petty C C, Politzer P A, Prater R and Rice B W 1999 *Plasma Phys. Control. Fusion* **41** B119
[44] Kernbichler W, Kapper G, Kasilov S V and Marushchenko N B 2016 *EPJ Web Conf.* **87** 01006
[45] Kapper G, Kasilov S V, Kernbichler W, Martitsch A F, Heyn M F, Marushchenko N B and Turkin Y 2016 *Phys. Plasmas* **23** 112511
[46] Ohkawa T 1976 Steady state operation of tokamaks by r-f heating *General Atomics Technical Report* GA-A13847 PB2000108008
[47] Taylor G, Efthimion P C, Kessel C E, Harvey R W, Smirnov A P, Ershov N M, Carter M D and Forest C B 2004 *Phys. Plasmas* **11** 4733
[48] Ram A K, Decker J and Peysson Y 2005 *J. Plasma Phys.* **71** 675
[49] Urban J, Decker J, Peysson Y, Preinhaelter J, Shevchenko V, Taylor G, Vahala L and Vahala G 2011 *Nucl. Fusion* **51** 083050